Land Surface–Induced Regional Climate Change in Southern Israel

KOEN DE RIDDER* AND HUBERT GALLÉE+

Institut d'Astronomie et de Géophysique G. Lemaître, Université Catholique de Louvain, Louvain-la-Neuve, Belgium

(Manuscript received 5 June 1997, in final form 23 January 1998)

ABSTRACT

Since the mid-1960s, the southern part of Israel has experienced major land use changes following the start of the irrigation scheme and the subsequent intensification of agricultural practice. Several studies, mainly based on the analysis of climatic time series, have shown that this has been followed by a significant change of the local climate, especially during the summer and early fall. They indicate a reduced diurnal amplitude of surface air temperature and wind speed, and a threefold increase of the October (early wet season) convective precipitation. In this paper, these phenomena are investigated by simulating the influence of the land surface on local meteorological variables with a two-dimensional version of a mesoscale atmospheric model containing a detailed land surface scheme. Particular attention is given to the correct estimation of land surface parameters from soil and vegetation maps and remote sensing data. The simulations confirm the observed reduction of the diurnal amplitude of temperature and wind speed when replacing a semiarid surface by a partly irrigated one. Furthermore, it is shown that the potential for moist convection increases with the surface moisture availability and is rather insensitive to the surface roughness.

1. Introduction

From April to October, the eastern Mediterranean is under the influence of a subtropical high pressure system, inhibiting rainfall almost completely and making nonirrigated agriculture possible only at the beginning of this period. Since June 1964 Israel has been operating the National Water System, transferring large amounts of water from Lake Tiberias (Yam Kinneret) (situated in the relatively wet north) to the dry regions of the south, thus making irrigated agriculture possible. This has led to intensified agricultural practice throughout the dry season, bringing about important land use changes. A significant fraction of the previously dry land is now cultivated, which has caused the surface roughness and the evapotranspiration to increase.

Several studies have shown that these land use changes have been followed by a local climate change. One of the first such studies was conducted by Alpert and Mandel (1986). They found a decreasing trend in the diurnal surface wind and temperature variabilities to be correlated with the enhanced irrigation. This was attributed to a decrease of the sensible heat flux (due to the irrigation) and the corresponding reduction of differential heating between land and sea, but they also mentioned the influence of roughness and albedo changes.

Otterman et al. (1990) observed a steep increase in the October rains (at the onset of the rainy season, when most rain is of convective origin) and attributed it to land use changes. They argued that the increased vegetation cover had lowered the surface albedo and the soil heat flux, resulting in an increased sensible heat flux. The related stronger convection could then more easily penetrate the capping inversion at the atmospheric boundary layer top and develop into convective rain. Note that there appears to be some confusion in this respect: whereas Alpert and Mandel (1986) conclude that a *decreased* sensible heat flux is causing the local climate to change, Otterman et al. (1990) invoke an *increased* sensible heat flux to explain the observed rainfall increase. Note, however, that the former study was dealing with the direct effect of irrigation, that is, the sensible heat flux decrease, whereas the latter was rather concerned with the effects of afforestation and the limitation on grazing of dormant vegetation, which one would indeed expect to increase the sensible heat flux near the end of the dry season.

Ben-Gai et al. (1993) also mentioned the different approaches regarding the role of the sensible heat flux in explaining regional climate change. In a study of the October rainfall patterns in southern Israel, they con-

* Current affiliation: VITO, Centre for Remote Sensing and Atmospheric Processes, Mol, Belgium.

+ Current affiliation: Center d'Etudes de la Neige, Grenoble, France.

Corresponding author address: Dr. Koen De Ridder, VITO, Centre for Remote Sensing and Atmospheric Processes, Boeretang 200, B-2400 Mol, Belgium.
E-mail: dridderk@vito.be

firmed the increasing trend in early seasonal rainfall. Furthermore, an analysis of the temporal and spatial rainfall patterns pointed to a distinct influence of land surface–related mesoscale effects, although changes in the synoptic pattern were not ruled out.

As far as southern Israel is concerned, it remains as yet unclear whether the observed increase of the October rains is consistent with a lower or a higher sensible heat flux. Therefore, we investigate how land use changes that have occurred in southern Israel during the last decades may have influenced the regional climate by means of simulations with a mesoscale atmospheric model, including a detailed land surface scheme. More specifically, we will focus on the near-surface meteorological variables and the potential for convective precipitation by running a simulation for 27 October 1990. A day in October was selected to perform the simulations because at the end of the dry season the effects of irrigation are expected to be the most significant and because the observed rainfall increase is most pronounced during this month. The reason to select this day in particular is that it produced the highest rainfall recording during that October month. Note that this same day has also been selected in other studies (P. Alpert 1995, personal communication). Because of the approximate meridional symmetry of the domain, simulations are performed in two dimensions.

Note that although this paper is concerned with only the influence of the land surface at the meteorological mesoscale, we do not exclude synoptic processes to play a role in explaining the increased precipitation. Indeed, there are indications (Steinberger and Gazit-Yaari 1996) that precipitation changes in southern Israel may be due to changes in the large-scale circulation. However, we do not address this issue here.

Extensive use will be made of the NOAA/NASA Pathfinder Advanced Very High Resolution Radiometer (AVHRR) Land (PAL) dataset (Agbu and James 1994) for the specification of some of the required land surface parameters, as well as for the retrieval of the land surface brightness temperatures.

This paper is organized as follows. Section 2 gives a description of the numerical model, the land surface parameters, and the initial conditions. In section 3 the coupled atmosphere–land surface model is validated through comparison of simulation results with surface meteorological data and satellite brightness temperatures for present-day conditions. In section 4 the simulations of the preceding section are repeated except that the surface parameters are chosen to be representative of the preirrigation conditions, and the results are compared with those of section 3 in order to demonstrate the influence of the land surface on near-surface meteorological parameters. Section 5 then describes a sensitivity study carried out in order to better understand the mechanisms that influence the potential for convective precipitation.

2. Model description

The model used to carry out the numerical simulations is the Modèle Atmosphérique Régional (MAR) (Gallée and Schayes 1994; Gallée 1995), a mesoscale atmospheric model developed at the Institut d'Astronomie et de Géophysique G. Lemaître from the model described in Alpert et al. (1982). This is a hydrostatic primitive equation model that employs the full continuity equation. The vertical coordinate is the so-called sigma coordinate, or terrain-following reduced pressure, which allows easy inclusion of topography. The model solves the prognostic equations of the wind, temperature, and moisture fields, together with the equation of state of ideal gases, on a numerical grid. The vertical subgrid-scale fluxes are computed with the $E - \epsilon$ turbulence model (Duynkerke 1988). The model contains two detailed radiation schemes: 1) Tricot and Berger (1988) as modified by Gallée et al. (1991) for the shortwave radiation and 2) a wideband formulation of the radiative transfer equation (Morcrette 1984) for the longwave radiation. It also contains a cloud microphysical model, which is essentially based on the Kessler (1969) parameterization. The model is three-dimensional but can be set to a one- or two-dimensional mode as well. A very simple fractional cloud cover scheme based on the relative humidity (RH) was added:

$$A_c = \frac{\mathrm{RH} - \mathrm{RH}_c}{\mathrm{RH}_m - \mathrm{RH}_c}, \tag{1}$$

with $\mathrm{RH}_c = 0.9 < \mathrm{RH} < \mathrm{RH}_m = 1.1$, $A_c(\mathrm{RH} < \mathrm{RH}_c) = 0$, and $A_c(\mathrm{RH} > \mathrm{RH}_m) = 1$. This function fits quite well with data presented in Ek and Mahrt (1991, their Fig. 7).

Surface fluxes of energy, water vapor, and momentum are computed with the land surface scheme described in De Ridder and Schayes (1997). Land surface heterogeneity at the subgrid scale is accounted for by allowing up to three vegetation types to coexist within a surface grid cell. In this approach [the mosaic approach; see Klink (1995) and references therein], energy and momentum fluxes are computed separately for each of the vegetation types and averaged with weighting coefficients proportional to the fraction of the corresponding surface cover.

The domain being studied is the agricultural area in southern Israel, a roughly 30-km-wide, north–south-oriented strip located between the cities of Tel Aviv (32°05′N, 34°45′E) and Beersheba (31°15′N, 34°45′E) (see Fig. 1). At the western side is the Mediterranean; at the eastern side and parallel to the region under study is a mountain ridge between 600 and 800 m high, beyond which lies the Dead Sea (Fig. 2). Note that in October the Mediterranean is still warm, making it an important moisture source.

Taking advantage of the approximate meridional symmetry of the domain, runs were performed with a two-dimensional version of the coupled atmosphere–land

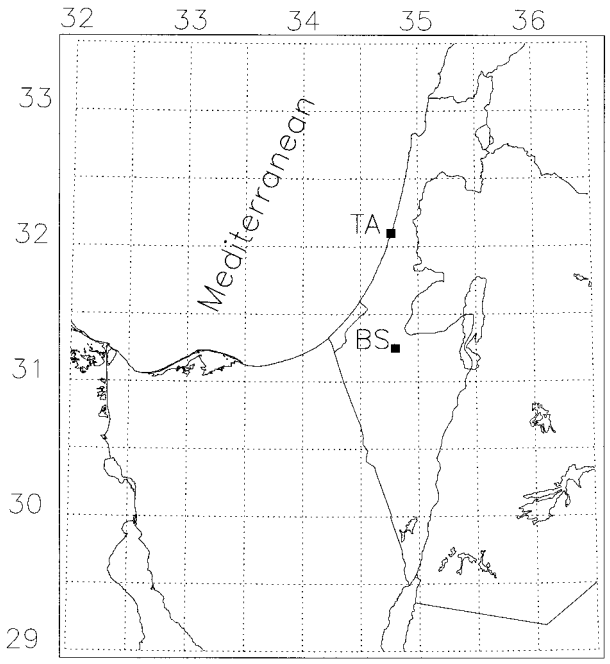

FIG. 1. Map of Israel and surroundings. The cities of Tel Aviv (TA) and Beersheba (BS) are indicated. Latitude and longitude are, respectively, at the left and upper side.

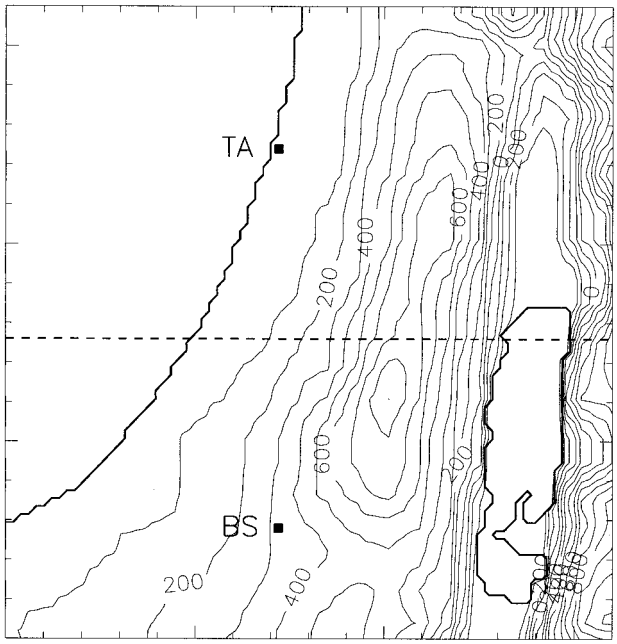

FIG. 2. Smoothed topography of southern Israel. Contour lines of height above sea level every 100 m. The distance between the ticks on the sides corresponds to a horizontal distance of 10 km. Note that the Dead Sea, at the lower-right corner, is located at an altitude of 400 m below sea level.

surface model in a vertical plane at a constant latitude (≈31°40′N), extending from 70 km offshore to 130 km inland. The vertical simulation plane is situated halfway between Tel Aviv and Beersheba, passing over the middle of the agricultural region of interest and roughly perpendicular to the mountain ridge (Fig. 2). Note that the simulation domain is situated in an area with relatively dark soils (with albedo values close to those of vegetation, i.e., in the 10%–20% range; see appendix A), meaning that the surface albedo is not very sensitive to vegetation cover changes. Therefore, we will not look at the effects of surface albedo but rather limit this study to the effects of surface moisture availability and roughness length.

The vertical resolution was defined as decreasing from 10 m at the ground to 2000 m at the model top located at 20-km altitude. The simulation employed 100 grid points in the horizontal direction and 30 in the vertical direction. The horizontal grid spacing is 2 km, which resolves the shallow thermal circulations that are expected to develop reasonably well and is still within the validity range of the hydrostatic approximation for this type of circulation (Pielke 1984). However, a hydrostatic model as the one used here is not appropriate to simulate deep convective motion because of the high vertical accelerations that may occur. Therefore, rather than simulating deep convection explicitly, the potential for convective precipitation will be predicted from vertical profiles of equivalent potential temperature and saturated equivalent potential temperature (see, e.g., Holton 1992). For a parcel of saturated air, the former is defined as

$$\theta_e = \theta \exp\left[\frac{L_v q_{\text{sat}}(T)}{c_p T}\right], \tag{2}$$

where θ is the potential temperature, L_v is the latent heat of condensation, $q_{\text{sat}}(T)$ is the saturated specific humidity at the parcel temperature T, and c_p is the specific heat. For a nonsaturated parcel, the saturated specific humidity can be replaced by the actual specific humidity if the temperature is replaced by T_{LCL}, the parcel's temperature at the lifting condensation level. The saturated equivalent potential temperature θ_{es} is defined as the equivalent potential temperature of a hypothetically saturated atmosphere that has the thermal structure of the actual atmosphere.

Based on information contained in land use maps (Richter 1981; Zohary 1981) and soil maps (FAO-UNESCO 1979), not shown here, the two-dimensional simulation domain was divided into areas with different surface characteristics (see Fig. 3). Between the Mediterranean and the Dead Seas one distinguishes the agricultural zone, followed by areas with evergreen trees, ground cover, and shrubs. The soil in the shrub-covered areas is defined as medium textured; everywhere else in the domain the soil is defined as fine textured. The FAO fine and medium textural classes were associated with, respectively, the clay and loam types of the United States Department of Agriculture (USDA) soil classi-

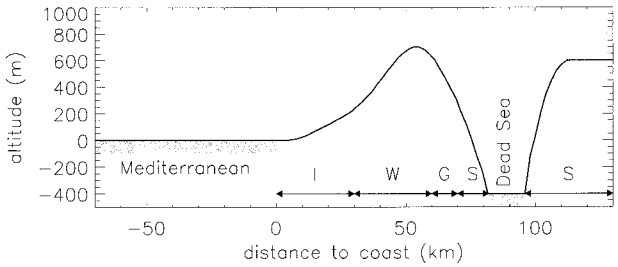

FIG. 3. The lower portion of the simulation domain. Legend: I is for irrigated crop and orchards, W is for evergreen woodland, G is for ground cover, and S is for shrubs.

fication since the land surface model makes use of the latter classification. The albedo of the bare soil was obtained from the National Oceanic and Atmospheric Administration/Advanced Very High Resolution Radiometer (NOAA/AVHRR) data, as explained in appendix A. Table 1 shows the parameter values used for the different soil and vegetation types used in the simulations.

The prognostic soil variables (temperature and volumetric soil moisture content) were initialized in a horizontally uniform way. The initial soil moisture for the irrigated vegetation (crops and orchards) was set to a value corresponding to a soil matric potential of −3.3 m, which allows abundant transpiration. The soil moisture outside the agricultural zone was initialized at the wilting point, that is, corresponding to a soil matric potential of −150 m. The soil temperature was initialized with observations from the Bet Dagan weather station. The sea surface temperature of the Mediterranean in October 1990 was 298 K (T. Ben-Gai 1996, personal communication), which is close to climatological values presented in Bottomley et al. (1990). Surface elevation was taken from the PAL ancillary data file and interpolated to a 2-km grid.

As stated in section 1, 27 October 1990 was chosen as the simulation day because it yielded the highest rainfall. To allow for some model adjustment, the simulations were started on 1800 LST 26 October. Radiosonde data taken at Bet Dagan, just south of Tel Aviv, served to uniformly initialize the vertical profiles of temperature, specific humidity, wind speed, and wind direction in the model (Fig. 4). The vertical wind profile is characterized by northwesterly flow in the lower levels and west-southwesterly flow at higher altitudes. Such a situation is quite typical for the eastern Mediterranean before the winter, as mentioned in Barry and Chorley (1992). Note that the low-level northwesterly flow advects humid air over the continent. Also note that the low-level air mass, after a journey over the relatively warm Mediterranean Sea, has developed a 1500-m-deep marine boundary layer with a distinct inversion aloft.

The domain characteristics and the initial conditions described here are common to all the simulations that are presented in the following sections. The only difference allowed for will be the specification of the vegetation characteristics of the agricultural zone between the coast and 30 km inland. Therefore, the specification of the vegetation in the agricultural zone will be done separately for every simulation.

3. Simulation of present-day conditions

The goal of the simulations that are shown here is to validate the coupled land surface–atmosphere model

TABLE 1. Vegetation and soil parameters used in the simulations. The different vegetation types are evergreen woodland (W), crops (C), ground cover (G), and shrubs (S). The terms ''vis'' and ''nir'' refer to the visible and near-infrared portions of the solar spectrum, respectively. The soil types ''medium'' and ''fine'' were associated with the USDA soil types ''loam'' and ''clay,'' respectively.

		Vegetation parameters			
Parameter	Description	W	C	G	S
z_{om} (m)	Roughness length momentum	1.5	0.05	0.02	0.1
d (m)	Displacement height	10.5	0.35	0.14	0.7
L (−)	Leaf area index (LAI)	6	4	4	1
ρ_{vis} (%)	Leaf reflectivity (live/dead)	10/16	11/36	11/36	10/16
ρ_{nir} (%)	Leaf reflectivity (live/dead)	45/39	58/58	58/58	45/39
τ_{vis} (%)	Leaf transmissivity (live/dead)	5/0	7/22	7/22	5/0
τ_{nir} (%)	Leaf transmissivity (live/dead)	25/0	25/38	25/38	25/0
g_v (−)	Green leaf fraction	1	1	0.2	0.2
r_0 (s m^{-1})	Minimum stomatal resistance	100	50	50	100
$\varphi_{0.1m}$ (−)	Root fraction upper 0.1 m soil	0.5	0.3	0.7	0.5
r_p (s)	Internal plant resistance	10^9	5×10^8	5×10^8	10^9
x_v (−)	Fractional vegetation cover	From satellite reflectances			

		Soil parameters	
Parameter	Description	Medium	Fine
η_{sat} (−)	Saturated water content	0.451	0.482
ψ_{sat} (m)	Water potential at saturation	−0.478	−0.405
K_{sat} (m s^{-1})	Hydraulic conductivity at saturation	7.0×10^{-6}	1.3×10^{-6}
b (−)	Water retention curve exponent	5.39	11.40
A_s (−)	Bare soil albedo	From satellite reflectances	

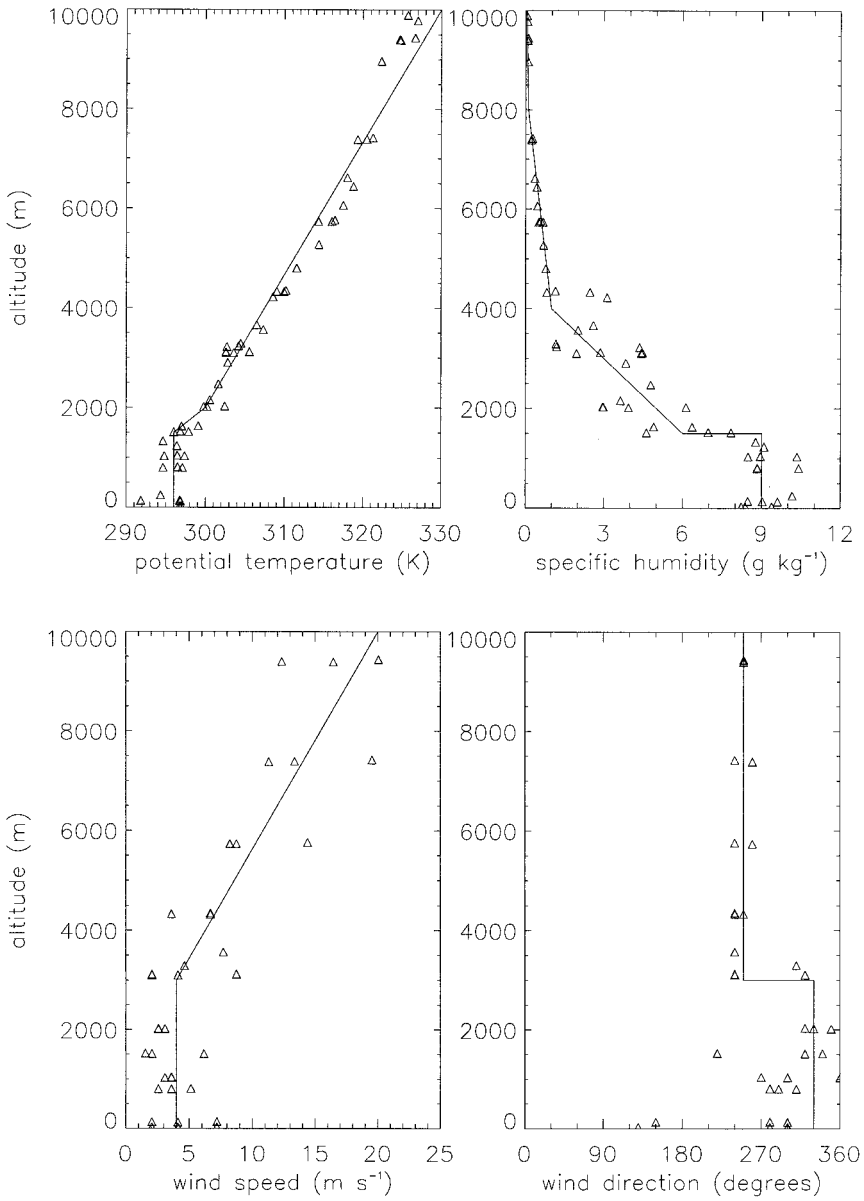

FIG. 4. Initial vertical profiles of potential temperature, specific humidity, wind speed, and wind direction. The triangles represent the radiosonde observations at 1300 LST 26 October and at 0100 and 1300 LST 27 October 1990. The full lines, fitted to the data by eye, are the vertical profiles used to initialize all model simulations in this study.

through intercomparison of simulation results for present-day conditions with observations and show the structure of the terrain-driven mesoscale circulations that develop. For the present-day simulations, the terrain characteristics and the initial conditions were taken as described in the previous section. The vegetation fraction per grid cell was obtained from NOAA/AVHRR data as explained in appendix A, yielding an average of about 32% cover in the agricultural zone.

Figure 5 shows the simulated near-surface values of temperature, humidity, wind speed, and wind direction at a point 15 km inland, as compared to 3-hourly measurements from synoptic weather stations at Bet Dagan and Lod Ben-Gurion, operated by the Israel Meteorological Service, located at 9 and 19 km inland, respectively. The simulated and observed temperatures at 2-m height are in excellent agreement. Both the amplitude and the phase of the diurnal temperature cycle are well reproduced by the model. The specific humidity at 2-m height is also in good agreement with the measurements, although slightly overestimated by the model. The simulated temperature and specific humidity at 2 m were

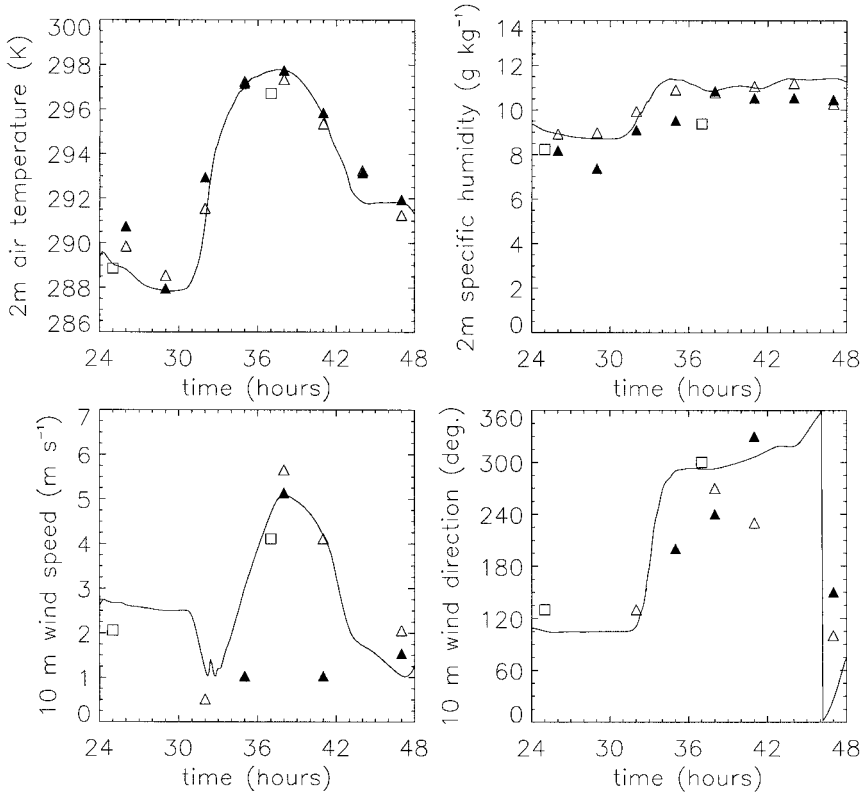

FIG. 5. Comparison of simulated (full line) with observed (triangles and squares) near-surface meteorological variables for 27 October 1990. The full triangles are data from Lod Ben-Gurion, the empty triangles are data from Bet Dagan, and the squares are data from the radiosounding's lowest level at Bet Dagan. The simulation results were taken at a point 15 km inland in the model domain, which is approximately halfway between Bet Dagan and Lod Ben-Gurion.

obtained by extrapolation from the first model level at 10 m using the Monin–Obukhov similarity theory for the nonneutral surface layer:

$$\theta_{2\mathrm{m}} = \theta_{10\mathrm{m}} + \frac{\theta_*}{k}\left[\ln\left(\frac{2\mathrm{m}}{10\mathrm{m}}\right) - \psi_H\left(\frac{2\mathrm{m}}{L}\right) + \psi_H\left(\frac{10\mathrm{m}}{L}\right)\right] \tag{3}$$

$$q_{2\mathrm{m}} = q_{10\mathrm{m}} + \frac{q_*}{k}\left[\ln\left(\frac{2\mathrm{m}}{10\mathrm{m}}\right) - \psi_H\left(\frac{2\mathrm{m}}{L}\right) + \psi_H\left(\frac{10\mathrm{m}}{L}\right)\right]. \tag{4}$$

The quantities θ_*, q_*, and L, used in the stability function ψ_H, represent the surface temperature scale, the humidity scale, and the Obukhov stability length $L = u_*^2\theta_0(kg\theta_*)^{-1}$, respectively. They were computed from the grid-averaged surface fluxes of heat and water vapor and the friction velocity u_* (Garratt 1992); here, θ_0 is a reference temperature. As to the comparison with the surface wind speed and direction at 10 m, note that the anemometers at the stations mentioned above do not respond to winds below 1–2 m s^{-1} and that their accuracy depends on instrument age and averaging period (S. Rubin 1996, personal communication). Nevertheless, the agreement between simulation and measurement is still quite satisfactory. The model clearly reproduces the observed diurnal cycle with low-speed southeasterly winds at night veering to northwesterly winds blowing with speeds up to 5–6 m s^{-1} during the day.

As a following step in the validation process, model-computed surface brightness temperatures were subjected to a comparison with satellite measurements from the PAL dataset. (Note that the term surface temperature refers to the surface skin temperature and not the surface air temperature.) Most surface temperature retrieval algorithms use the split-window technique, which is based on the differential absorption, mainly by water vapor, between AVHRR channels 4 and 5. However, a serious drawback of this method is that the difference in brightness temperature between both channels is not only affected by atmospheric water vapor but also by spectral emissivity differences. These may be important for sparsely vegetated surfaces such as those that exist in southern Israel. Therefore, we have preferred to use an atmospheric correction formula that is solely based on

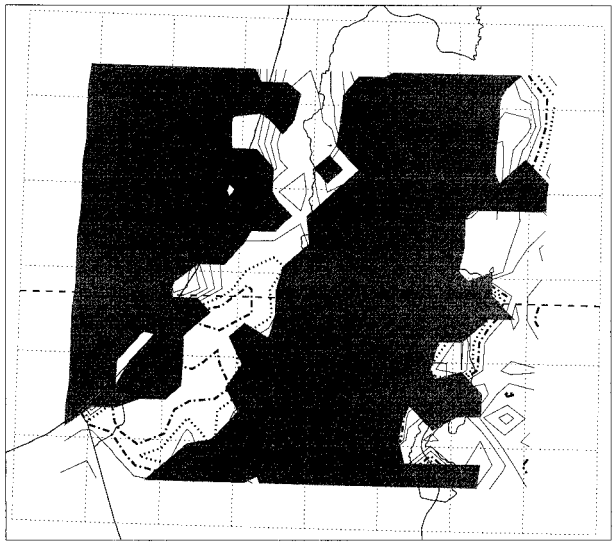

FIG. 6. Observed land surface temperature at approximately 1400 LST 27 October 1990. The dash–dot line and the dashed line are the 305- and 306-K contour lines, respectively. Cloudy areas are shown in gray.

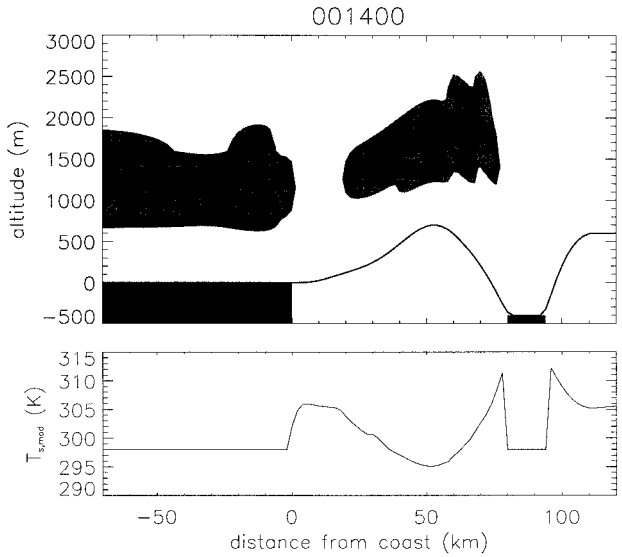

FIG. 7. Simulated cloudiness (upper panel) and surface brightness temperature (lower panel) at 1400 LST. Regions with a cloudiness higher than 10% are shown in light gray.

the amount of water vapor in the atmosphere. Such a formula can be obtained by combining Dalu's (1986) precipitable water content retrieval formula,

$$W = 19.6\ kg\ \mathrm{m}^{-2}\ \mathrm{K}^{-1} \times (T_4 - T_5)\cos\theta_v, \quad (5)$$

with Price's (1984) surface brightness temperature retrieval formula

$$T_{s,\mathrm{sat}} = T_4 + 3.33(T_4 - T_5), \quad (6)$$

with θ_v the satellite view angle and T_i ($i = 4, 5$) the brightness temperature in AVHRR channel i. The result is given by

$$T_{s,\mathrm{sat}} = T_4 + \frac{3.33W}{19.6\ kg\ \mathrm{m}^{-2}\ \mathrm{K}^{-1} \times \cos\theta_v}. \quad (7)$$

Figure 6 shows the spatial distribution of the surface brightness temperature obtained by means of (7) from satellite measurements contained in the NOAA/National Aeronautics and Space Administration (NASA) Pathfinder AVHRR Land dataset (Agbu and James 1994) for southern Israel at 1400 LST 27 October. The value of $W = 32$ kg m^{-2} was obtained from the 1300 LST radio sounding at Bet Dagan. The surface temperature in the agricultural zone halfway between Tel Aviv and Bet Dagan exhibits values between 305 and 306 K. Cloud cover, obtained from the cloud flag in the PAL dataset and represented by the gray shading in Fig. 6, occurs over the mountain ridge and near the coastline.

Note that (7) yields the surface brightness temperature, which differs from the thermodynamic temperature for nonperfect absorbers. Therefore, the (corrected) satellite brightness temperature was compared with the modeled surface brightness temperature, which is defined as

$$T_{s,\mathrm{mod}} = \left(\sum_k x_k \epsilon_k T_k^4\right)^{1/4}, \quad (8)$$

where ϵ_k is the emissivity and T_k is the thermodynamic temperature of surface type k, occupying a fraction x_k of a model grid cell. In the land surface model used in this study, the emissivity values are fixed at $\epsilon_g = 0.94$ for bare soil and $\epsilon_v = 0.98$ for vegetated surfaces. The modeled cloudiness and surface brightness temperature are shown in Fig. 7. There is a striking similarity between the simulated and observed cloudiness: in both cases clouds are apparent over the mountain ridge and near the coastline, leaving a cloud-free region approximately 20 km wide. In this cloud-free region, the simulated surface brightness temperatures are between 305 and 306 K, which is in excellent agreement with the satellite measurements. Note that the quasi-meridional symmetry of the satellite image (Fig. 6), together with the capacity of the model to reproduce these observations, strongly supports the correctness of the two-dimensional approach.

The simulation presented in this section exhibits some typical mesoscale phenomena, mainly due to the strong local forcing provided by the mountain ridge and the land–sea temperature contrast. During the night a combined katabatic–land breeze develops (Fig. 8). This circulation brings down cold, dry air from high on the mountain ridge in a shallow layer. The properties of the descending air mass strongly contrast with the warm and humid low-level prevailing flow. This downslope flow persists until midmorning, when the heating of the land surface has created a large enough opposite pressure gradient in order for the flow direction to be reversed. Now a combined sea–mountain breeze develops

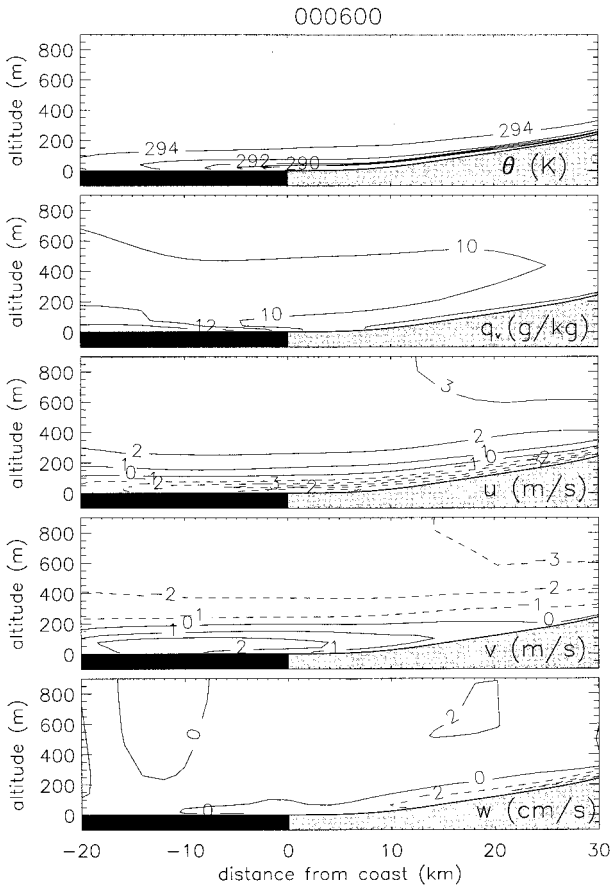

FIG. 8. Simulated atmospheric fields at 0600 LST for a portion of the simulation domain situated near the coast. From the top downward are shown the potential temperature (K), specific humidity (g kg^{-1}), the horizontal wind speed component parallel to the simulation plane (m s^{-1}), the horizontal wind speed component perpendicular to the simulation plane (m s^{-1}), and the vertical wind speed (cm s^{-1}). Negative wind speed values are indicated by a dashed line.

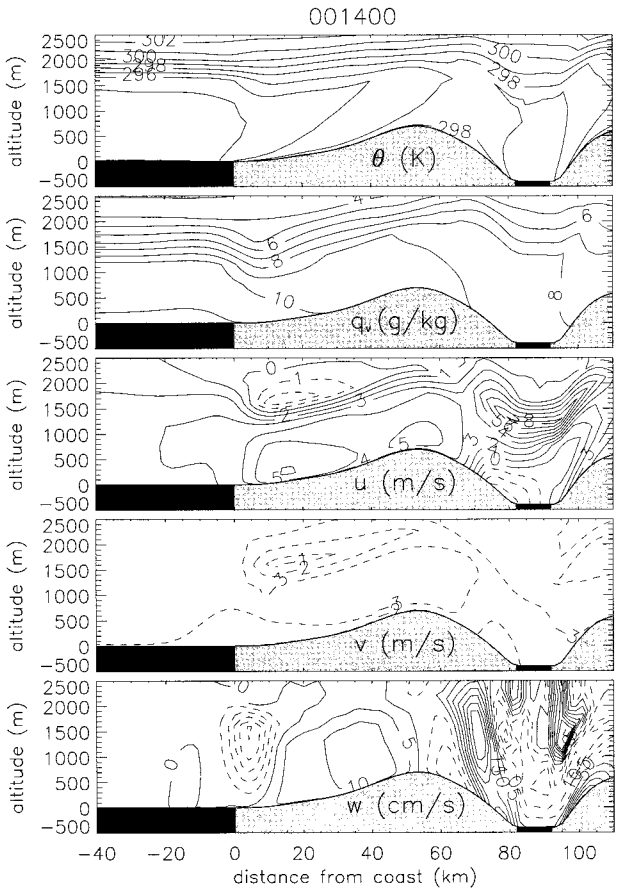

FIG. 9. As in Fig. 8, but at 1400 LST and showing almost the entire domain.

(Fig. 9) with air rising above the mountain ridge and subsidence above the agricultural zone. This flow pattern is consistent with the observed cloudiness pattern (Fig. 6) since downward motion generally inhibits the formation of clouds.

4. Simulation of preirrigation conditions

To assess the influence of the land use changes in southern Israel, a run was performed under exactly the same conditions as described in the previous section, except for the fact that the irrigated vegetation was replaced by a 10% cover of small, dry bushes, as representative of the preirrigation situation. This change results in an increase of the sensible heat flux and an according decrease of the latent heat flux by about 75 W m^{-2} (Fig. 10) at midday. This may seem small, but recall from the previous section that the land use change only affects 32% of the surface in the simulation.

Figure 11 shows the impact on the near-surface meteorological variables. The diurnal amplitude of temperature and wind speed are seen to increase, as was also observed by Alpert and Mandel (1986). As far as the wind speed is concerned, the increase is mainly produced during the day, which can be explained by the reduced surface roughness as well as the higher land–sea thermal contrast. The increase of the temperature amplitude is, somewhat surprisingly, largely due to cooler temperatures at the end of the night rather than to an increase of the daytime temperature, as one would expect. The cooler temperatures at night can be explained by the fact that the lower surface roughness produces less vertical mixing. This limits entrainment of warm air from the residual neutral boundary layer into the stable nocturnal layer close to the surface. The lower-than-expected daytime temperature increase has two causes. First, the heat injected into the atmosphere at the surface is quickly distributed over the entire convective boundary layer, which, because of its depth (1500 m), has a considerable heat-absorbing capacity. Second, in the case of a dry surface the wind speed is higher, and, as a consequence, an air mass subjected to surface heating warms up less, as can be deduced from (B7).

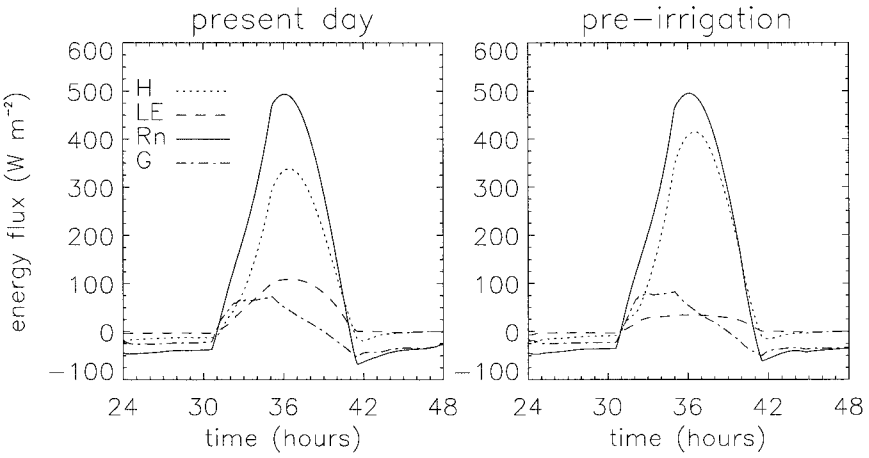

FIG. 10. Simulated surface energy fluxes for present-day (left) and preirrigation (right) conditions at a point 15 km inland. Shown are the sensible heat flux (H), the latent heat flux (LE), the net radiation flux (R_n), and the heat storage flux (G).

Figure 12 shows the vertical θ_e and θ_{es} profiles for both present-day and preirrigation conditions for a point 15 km inland at 2300 LST. This particular time was chosen because it is the moment at which saturation first occurs in the present-day simulation at around 1-km height. Since the atmosphere is conditionally unstable at this level ($\partial\theta_{es}/\partial z < 0$) (see, e.g., Holton 1992), moist convection and associated precipitation are bound to develop. In the preirrigation simulation, on the other hand, saturation does not take place. Therefore, we conclude that the present-day situation is more prone to moist convection and that the introduction of irrigated fields in the arid zones of southern Israel has led to an enhanced potential for convective precipitation. Note

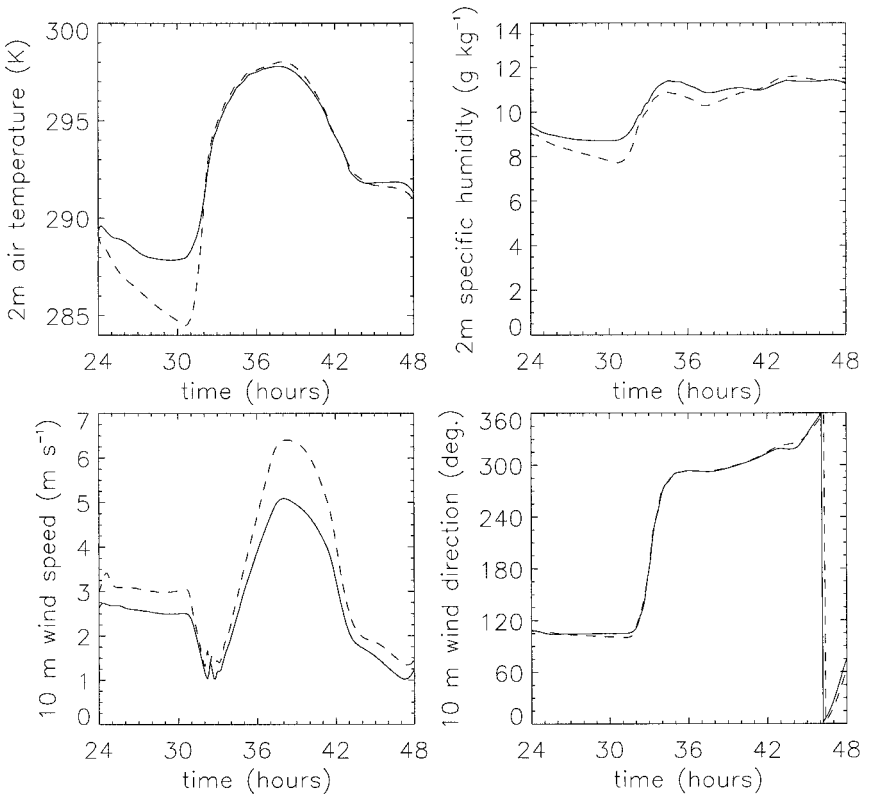

FIG. 11. Simulated surface meteorological variables for present-day (solid line) and preirrigation (dashed line) conditions at a point 15 km inland.

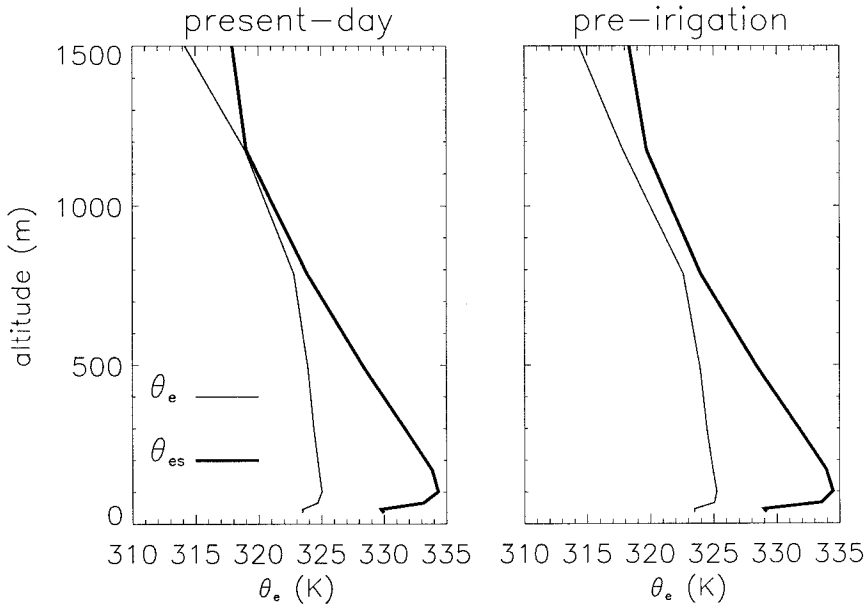

FIG. 12. Vertical profiles of simulated equivalent potential temperature and saturated equivalent potential temperature for present-day (left) and preirrigation (right) conditions for a point 15 km inland at 2300 LST.

that the difference between the profiles in Fig. 12 is rather small. However, in areas where convection is marginal such differences may be significant. A discussion regarding the causes of the different θ_e profiles is given in the following section.

5. Sensitivity study

As previously shown, land use changes that have occurred in southern Israel affect not only the near-surface meteorological variables but also the vertical profiles of equivalent potential temperature in such a way as to enhance the potential for deep convection. However, as far as the latter is concerned it is not clear which surface parameter is responsible. Therefore, a sensitivity study was carried out by running a series of simulations with drastically different parameters in the agricultural zone. The goal is to study the effect of changing conditions in the agricultural zone in a selective way by modifying one parameter at a time without affecting the others, allowing the isolation of the possible causes of the enhanced potential for convective precipitation.

Two surface parameters are believed to have the potential to influence the mesoscale circulation being studied here: the roughness length and the moisture availability. The albedo is not considered since, as explained above, the agricultural areas are dominated by dark soils, such that the surface albedo is only marginally affected by the vegetation cover. Of course, this limits the results of our study to the dark soil areas and excludes the bright soil regions in the southern part of the domain (see appendix A). For the purpose of this sensitivity study, a vegetation type was defined as having the properties of crop (see Table 1), except for the roughness length, which was set to either 0.01 or 1 m. These values, on either side of the range that is representative for most land surfaces, were chosen to be sufficiently different to provide significantly different forcings. Furthermore, two different soil moisture availabilities were defined, corresponding to wilting point (i.e., dry) and field capacity (i.e., wet), respectively. The combination of the two vegetation types with the two moisture availability conditions yielded the following combinations: 1) low moisture availability and low roughness (LMLR), 2) low moisture availability and high roughness (LMHR), 3) high moisture availability and low roughness (HMLR), and 4) high moisture availability and high roughness (HMHR). The diurnal evolution of the turbulent surface energy fluxes for a point 15 km inland is shown for all four cases in Fig. 13.

The results of the sensitivity runs were analyzed by means of the factor separation method (Stein and Alpert 1993). Applied to the simulation results presented here, this method allows us to quantify the separate effects of surface roughness and moisture availability, as well as their combined effect. The method was applied to the simulated vertical velocity field, taking the LMLR simulation as control run. Given the two forcings, surface roughness and moisture, and given the four simulations (LMLR, LMHR, HMLR, and HMHR), factor separation produces the following vertical velocities:

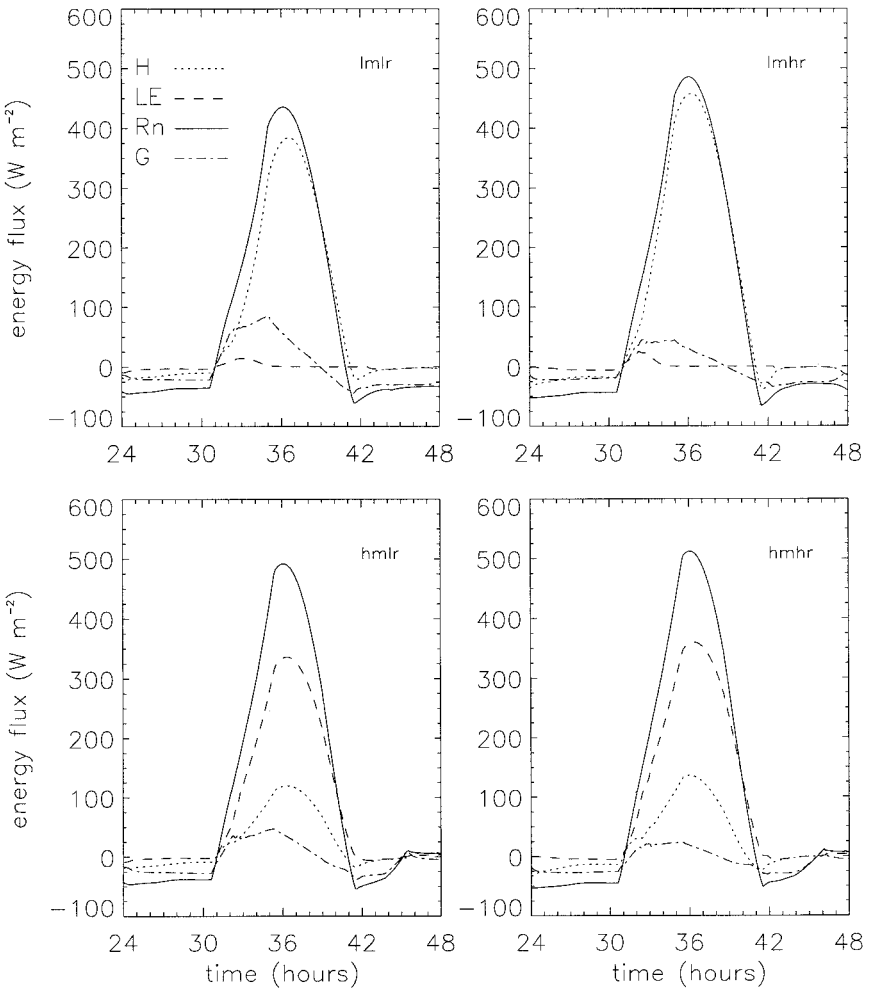

FIG. 13. Diurnal evolution of the surface energy fluxes for the different sensitivity simulations at a point 15 km inland.

$$\hat{w}_{\mathrm{CTRL}} = w_{\mathrm{LMLR}}, \tag{9}$$

$$\hat{w}_R = w_{\mathrm{LMHR}} - w_{\mathrm{LMLR}}, \tag{10}$$

$$\hat{w}_M = w_{\mathrm{HMLR}} - w_{\mathrm{LMLR}}, \tag{11}$$

and

$$\hat{w}_{RM} = w_{\mathrm{HMHR}} - (w_{\mathrm{LMHR}} + w_{\mathrm{HMLR}}) + w_{\mathrm{LMLR}}. \tag{12}$$

These variables are shown in Fig. 14 at 1500 LST. The upper panel shows $\hat{w}_{\mathrm{CTRL}}$, which is simply the vertical velocity of the control run (LMLR). The vertical velocity pattern corresponds to the situation of a combined sea–mountain breeze (as discussed above) with an ascending branch above land and descending motion just offshore. The second panel shows $\hat{w}_R$, which is the deviation from the control run due to the effect of the increased surface roughness. A threshold of ± 4 cm s^{-1} was used in the display of the vertical velocities, and it is very clear that the effect of roughness is almost nonexistent. Surface moisture, on the contrary, has quite an impact on the vertical velocity, as shown in the third panel. The positive values of $\hat{w}_M$ at approximately the same position as the downward branch of the control run virtually annihilate the vertical velocity, meaning that the downward velocity just offshore for the moist run is much reduced relative to the control run. The lower panel, showing $\hat{w}_{RM}$, reveals that the interaction of surface roughness and moisture has a negligible impact on the vertical velocity.

There is a stronger downward motion near the coast for low moisture availability as compared to the high moisture availability in the simulation results. The obvious reason is that a dry surface causes much greater heating of the atmosphere adjacent to the sea, and therefore a stronger circulation is generated in response to the stronger thermal gradient. As a result, in the case of a dry coastal zone there is a larger downward transport of dry and warm air from above the boundary layer. Later in the afternoon, the atmospheric vertical structure, shaped by the downward transport of dry air, is

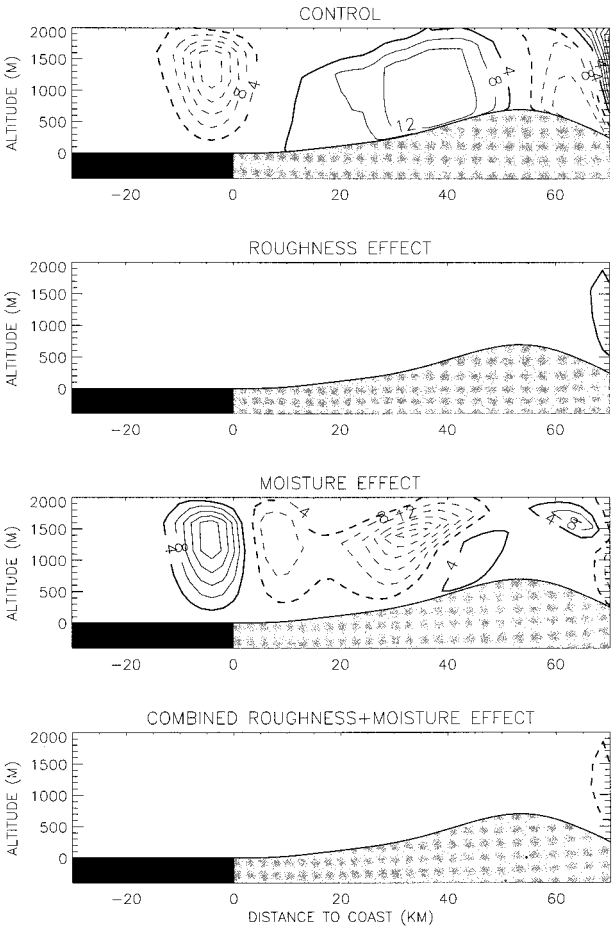

FIG. 14. The factor separation method applied to the simulated vertical velocity field at 1500 LST. From the top downward are shown $\hat{w}_{\mathrm{CTRL}}$, $\hat{w}_R$, $\hat{w}_M$, and $\hat{w}_{RM}$, respectively.

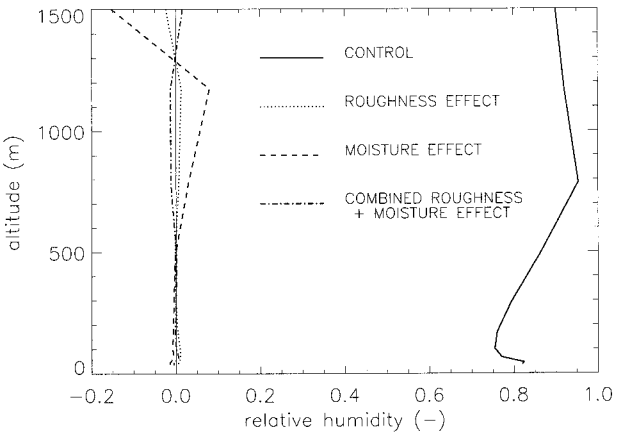

FIG. 15. The factor separation method applied to the simulated vertical profiles of relative humidity at a point 15 km inland at 2100 LST. The solid line is the relative humidity of the control run. The dotted line is the impact of the surface roughness, the dashed line is the impact of the surface moisture, and the dash–dot line is the combined impact of roughness and moisture.

advected over the coastal area by the onshore flow. This happens rather slowly because the component of the horizontal wind speed perpendicular to the coastline is small, especially near the boundary layer top. The resulting vertical profiles of relative humidity at 2100 LST for a point 15 km inland are shown in Fig. 15 for all four simulated cases. The effect of high surface humidity is to increase the humidity of the upper part of the boundary layer. This is not so much because more moisture is injected in the atmosphere, as in the case of a wet coastal zone. It is because of the effect of the surface dryness upon the strength of the circulation and, in particular, the magnitude of the downward velocity. From Fig. 15 note that the moist simulations exhibit layer saturation near the boundary layer top, which, in combination with the conditionally unstable stratification of the overlying air mass, would lead to moist convection. The dry simulations, in contrast, do not exhibit layer saturation. Under such circumstances moist convection does not take place, unless of course a large enough vertical velocity perturbation (e.g., associated with a frontal passage) were to uplift the upper boundary layer air and cause saturation.

Inspection of Figs. 14 and 15 also reveals that the velocity and humidity fields are rather insensitive to the surface roughness, despite a difference of two orders of magnitude in the roughness lengths used. To better understand this phenomenon, a simple scale analysis was performed. Assuming hydrostatic balance in the boundary layer (of depth h), together with the observation that the mesoscale pressure gradient must be zero close to the boundary layer top because of the reversal of the flow direction there, the pressure gradient force in the uphill direction can roughly be estimated as follows:

$$-\frac{1}{\rho_0}\frac{\partial p}{\partial x} \approx \frac{1}{2}\frac{1}{\rho_0}\frac{\partial}{\partial x}(\overline{\rho}\, gh), \tag{13}$$

$$\approx \frac{1}{2}h\frac{g}{\theta_0}\frac{\partial \overline{\theta}}{\partial x}. \tag{14}$$

The overlines denote boundary layer vertical averages. The factor ½ reflects the fact that the pressure gradient force varies linearly between a zero value at the boundary layer top and a maximum value at the surface, which has a net effect of half the maximum pressure gradient force on the boundary layer air mass. The temperature gradient following the x direction can be estimated by assuming that an air parcel, extending vertically over the entire boundary layer, moves over the surface at a uniform speed u and is thereby heated from below by the sensible heat flux $\overline{w'\theta'}$. In appendix B it is shown that in the early afternoon

$$\frac{\partial \overline{\theta}}{\partial x} = \frac{\overline{w'\theta'}}{uh}. \tag{15}$$

Substituting (15) into (14) yields

$$-\frac{1}{\rho_0}\frac{\partial p}{\partial x} \approx \frac{1}{2}\frac{g}{\theta_0}\frac{\overline{w'\theta'}}{u}. \quad (16)$$

The frictional force in the uphill direction can also be assessed in a simple manner. Neglecting the drag at the top of the boundary layer, it can be written as $C_d u^2 h^{-1}$, where C_d is a surface drag coefficient. Inserting representative values for the different variables ($\overline{w'\theta'} \approx 0.3$ K m s^{-1}, $u \approx 5$ m s^{-1}, $C_d \approx 0.005$, and $h \approx 1250$ m), one obtains

$$-\frac{1}{\rho_0}\frac{\partial p}{\partial x} \approx 10^{-3} \text{ m s}^{-2} \quad (17)$$

and

$$\frac{C_d u^2}{h} \approx 10^{-4} \text{ m s}^{-2}, \quad (18)$$

showing that the thermally induced mesoscale acceleration is an order of magnitude more important than the frictional force, thus explaining the flow's insensitivity with respect to the surface roughness.

6. Conclusions

In this paper the effect of recent land use changes in southern Israel on the local climate was studied by means of numerical simulations with a two-dimensional version of the mesoscale atmospheric model MAR. A significant effort was made to obtain realistic land surface parameters. In a validation study, it was shown that the two-dimensional version of the MAR is capable of reproducing observed variables (near-surface meteorological variables, cloud patterns, and surface brightness temperatures) for the current case. Typical mesoscale circulations developed in response to the topographical forcing.

Comparison of simulation results representative for the periods before and after the start of the irrigation program indicated that the irrigation and the enhanced cultivation in southern Israel have reduced the diurnal amplitude of wind speed and temperature. From inspection of the vertical profiles of equivalent potential temperature, it was found that the effect of irrigation is also to increase the potential for moist convection.

Finally, a series of sensitivity studies showed that changing a dry surface into a moist surface in southern Israel's coastal zone reduces the downward transport of dry air into the marine boundary layer, creating a vertical atmospheric structure that favors moist convective activity. It is important to note that is not the direct effect of the increased injection of moisture in the atmosphere at the surface that causes the increased potential for convective precipitation, but rather a dynamic effect associated with the decreased surface sensible heat flux and consequent decreased strength of the coastal circulation. It was also found that the potential for moist convection exhibits a much smaller sensitivity to the surface roughness than to the direct thermal effect of the irrigation.

In this work we have examined the effect of the land use changes on the thermodynamic structure of the atmosphere for only a single day, although the meteorological conditions on this day are quite representative for the time of the year considered. Future work should include three-dimensional modeling with explicitly computed precipitation, longer time periods and different years, and the relative importance of large-scale versus local forcings upon the convective precipitation in southern Israel.

Acknowledgments. We would like to thank P. Alpert for suggesting the subject, T. Ben-Gai for lively discussions, F. Nachtergaele for the digital version of the FAO-UNESCO *Soil Map of the World,* S. Rubin for assistance with the data of the Israel Meteorological Service, D. Tanré for providing the 6S radiative transfer code, and B. Teng for providing the PAL data. Thanks also to E. Lambin, M. Lopez-Novella, A. Quinet, G. Schayes, A. Sneessens, and M. Verstraete for comments on an early version of the manuscript. Hubert Gallée acknowledges support of the Programme Antarctique Belge (Contract a4/DD/E01), and Koen De Ridder acknowledges support of the Fonds pour la Formation a la Recherche dans l'Industrie et dans l'Agriculture (FRIA).

APPENDIX A

Vegetation Fraction and Bare Soil Albedo from NOAA AVHRR

The vegetation fraction per grid cell and the bare soil albedo were estimated from satellite reflectances contained in the composite files of the NOAA/NASA Pathfinder AVHRR Land (PAL) dataset (Agbu and James 1994). In order to remove residual cloud contamination, the three 10-day composites of October 1990 were further composited (Holben 1986) to 1 month. The correction for the remaining atmospheric effects (absorption by ozone and water vapor, and Rayleigh and aerosol scattering) was performed by means of the radiative transfer model 6S, an updated version of the 5S model (Tanré et al. 1990). The 6S model was used in a reverse mode to compute the ground surface reflectance from the observed top-of-atmosphere reflectance. The required input data were obtained from data files of the synoptic weather station at Bet Dagan, either directly (columnar precipitable water content) or indirectly (visibility was used instead of aerosol optical depth). Corrections for the anisotropy of the surface reflectance were done by means of the Rahman et al. (1993) semiempirical model.

A simple procedure was then employed to compute the bare soil albedo and the vegetation fraction per grid cell from the corrected red and near-infrared reflectances

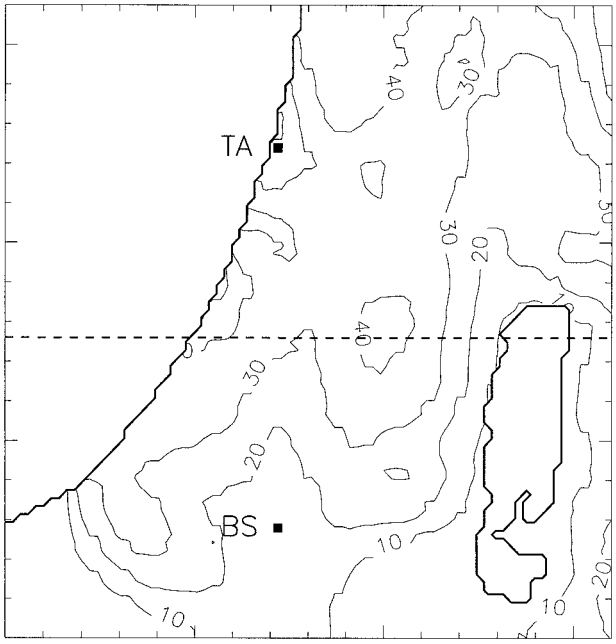

FIG. A1. Fractional vegetation cover x_v (%). Based on data from the NOAA/NASA Pathfinder AVHRR Land (PAL) dataset (Agbu and James 1994).

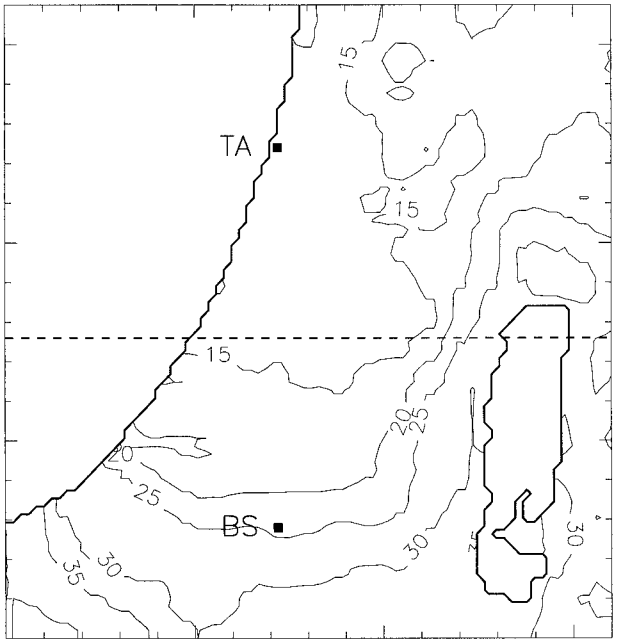

FIG. A2. Bare soil albedo A_s (%). Based on data from the NOAA/NASA Pathfinder AVHRR Land (PAL) dataset (Agbu and James 1994).

for all the PAL bins covering the domain of interest. In this procedure the assumption was made that patches of bare soil and dense vegetation occur together within each bin. This has the advantage of being compatible with the mosaic-type approach employed in the land surface model. Using prescribed plant hemispherical reflectances, one can then express the observed surface reflectances as a weighted sum of the reflectances of the bare soil and the vegetated surface, where the weights are proportional to the occupation fractions

$$\rho_1 = x_v\rho_{v1} + (1 - x_v)0.9A_s, \quad \text{(A1)}$$

$$\rho_2 = x_v\rho_{v2} + (1 - x_v)1.1A_s. \quad \text{(A2)}$$

In these equations, ρ_{vi} is a prescribed vegetation-type-dependent reflectance and $i = 1, 2$ stands for the AVHRR channels 1 and 2. The variable x_v is the fraction of the surface covered by vegetation, and A_s is the broadband hemispherical reflectance of the bare soil; both are defined for each bin of the satellite image. The coefficients in front of A_s (0.9 and 1.1) were chosen in such a way that they yield a bare soil NDVI [normalized difference vegetation index, defined as $(\rho_2 - \rho_1)/(\rho_2 + \rho_1)$] of 0.1, which is approximately the lowest value of the NDVI encountered (i.e., attributable to bare soil) on the satellite images of southern Israel.

The system of Eqs. (A1) and (A2) was then solved for each PAL bin of the domain using the corrected satellite reflectances ρ_i and prescribing the vegetation reflectances ρ_{vi}. The latter were computed for each vegetation type present in the domain by means of the radiation subscheme (De Ridder 1997) of the land surface model used in the simulations using parameter values listed in Table 1.

The fractional vegetation cover obtained this way (Fig. A1) exhibits features that are consistent with existing land use maps (Richter 1981; Zohary 1981), such as the scarceness of vegetation south of Beersheba and around the Dead Sea. As for the agricultural zone along the coast, which is of interest in this study, the fractional vegetation cover exhibits values between 25% and 40%.

Qualitative confirmation of the correctness of the bare soil albedo map (Fig. A2) was found in the FAO-UNESCO *Soil Map of the World* (FAO-UNESCO 1979). Although this map does not contain specific information about the albedo of the soil types present in southern Israel, it gives a soil color indication for similar soils elsewhere that underwent thorough surveys. The comparison of the soil albedo produced by the method described in this section with the FAO map was favorable, showing that the method was capable of identifying the dark soils in the agricultural zone between Tel Aviv and Beersheba, and the brighter soils around the Dead Sea and the regions south and west of Beersheba. Note further that the large range of albedo values encountered in Fig. A2 is supported by Mandel and Mahrer (1995), who report soil albedos between 10% and 38%. An important consequence is that in regions with dark soils the surface albedo is not much different from the bare soil albedo (both are in the 10%–20% range), meaning that enhanced vegetative cover has only limited consequences for the surface albedo there. (Note the difference between *bare soil* and *surface* albedo, the

latter being the average albedo of the surface with vegetation and the former the albedo of the surface if all vegetation were to be removed.) However, enhanced vegetative coverage in the regions with light soils should have a noticeable effect on the surface albedo, as for instance in the agricultural zone west of Beersheba.

APPENDIX B

Computation of $\partial\overline{\theta}/\partial x$

Consider an air parcel, extending vertically over the entire convective boundary layer of depth h, moving at a uniform speed u along the x axis, which is chosen perpendicular to the coastline, directed inland, and with origin at the coast. It is assumed that the parcel's potential temperature $\overline{\theta}$ is well mixed in the vertical. When heated from below by a time-dependent sensible heat flux of the form $(\overline{w'\theta'})_0 \sin\omega t$ [where $\omega = 2\pi T^{-1}$ and $T = 86\,400$ s, t is the time counted from the moment that the sensible heat flux becomes positive in the morning, and $(\overline{w'\theta'})_0$ is the noon value of the sensible heat flux] the conservation of energy for this parcel can be written as

$$\frac{\partial\overline{\theta}}{\partial t} + u\frac{\partial\overline{\theta}}{\partial x} = \frac{(\overline{w'\theta'})_0}{h}\sin\omega t. \tag{B1}$$

This equation can be solved by the Laplace transform method (see, e.g., Pipes and Harvill 1971). To do so, we define the Laplace transform of the boundary layer potential temperature as $\tilde{\theta}(x, s) = \mathcal{L}[\overline{\theta}(x, t)]$. Applying the Laplace transform to (B1) and defining $\theta_0 = \overline{\theta}(0, t) = \overline{\theta}(x, 0)$ reduces this equation to an ordinary differential equation:

$$s\tilde{\theta} - \theta_0 + u\frac{\partial\tilde{\theta}}{\partial x} = \frac{(\overline{w'\theta'})_0}{h}\frac{\omega}{s^2 + \omega^2} \tag{B2}$$

with solution

$$\tilde{\theta}(x, s) = \frac{\theta_0}{s} + \frac{(\overline{w'\theta'})_0}{hs}\frac{\omega}{s^2 + \omega^2}(1 - e^{-sx/u}). \tag{B3}$$

The reverse transform of (B3) yields

$$\overline{\theta}(x, t) = \theta_0 + \frac{(\overline{w'\theta'})_0}{h\omega}\left\{(1 - \cos\omega t) - H\left(t - \frac{x}{u}\right) \times\left[1 - \cos\omega\left(t - \frac{x}{u}\right)\right]\right\}, \tag{B4}$$

where $H(\cdot)$ is the Heaviside stepfunction, which is equal to one for a positive argument and equal to zero for a negative argument. For $x \approx 15\,000$ m and $u \approx 5$ m s^{-1}, the argument becomes positive after approximately 1 h. In that case one has

$$\overline{\theta}(x, t) = \theta_0 + \frac{(\overline{w'\theta'})_0}{h}\frac{1}{\omega}\left[\cos\omega\left(t - \frac{x}{u}\right) - \cos\omega t\right], \tag{B5}$$

and thus

$$\frac{\partial\overline{\theta}}{\partial x} = \frac{(\overline{w'\theta'})_0}{uh}\sin\omega\left(t - \frac{x}{u}\right). \tag{B6}$$

The sine function reaches a maximum at $t = 0.25T + xu^{-1}$, which is approximately at 1300 LST for the x and u values given previously. At this time of the day the horizontal gradient of the boundary layer potential temperature is therefore given by

$$\frac{\partial\overline{\theta}}{\partial x} = \frac{(\overline{w'\theta'})_0}{uh}. \tag{B7}$$

REFERENCES

Agbu, P. A., and M. E. James, 1994: The NOAA/NASA Pathfinder AVHRR land data set user's manual. Goddard Space Flight Center, Greenbelt, MD, 94 pp. [Available from Goddard Distributed Active Archive Center, User Services Offices, Code 902.2, Global Change Data Center, NASA/GSFC, Greenbelt, MD 20771.]

Alpert, P., and M. Mandel, 1986: Wind variability—An indicator for a mesoclimatic change in Israel. *J. Climate Appl. Meteor.*, **25,** 1568–1576.

——, A. Cohen, J. Neumann, and E. Doron, 1982: A model simulation of the summer circulation from the eastern Mediterranean past Lake Kinneret in the Jordan Valley. *Mon. Wea. Rev.*, **110,** 994–1006.

Barry, R. G., and R. J. Chorley, 1992: *Atmosphere, Weather and Climate.* Routledge, 392 pp.

Ben-Gai, T., A. Bitan, A. Manes, and P. Alpert, 1993: Long-term change in October rainfall patterns in southern Israel. *Theor. Appl. Climatol.*, **46,** 209–217.

Bottomley, M., C. K. Folland, J. Hsiung, R. E. Newell, and D. E. Parker, 1990: *Global Ocean Surface Temperature Atlas.* United Kingdom Meteorological Office, 20 pp. and 313 plates.

Dalu, G., 1986: Satellite remote sensing of atmospheric water vapor. *Int. J. Remote Sens.*, **7,** 1089–1097.

De Ridder, K., 1997: Radiation transfer in the IAGL land surface model. *J. Appl. Meteor.*, **36,** 12–21.

——, and G. Schayes, 1997: The IAGL land surface model. *J. Appl. Meteor.*, **36,** 167–182.

Duynkerke, P. G., 1988: Application of the $E - \epsilon$ turbulence closure model to the neutral and stable atmospheric boundary layer. *J. Atmos. Sci.*, **45,** 865–880.

Ek, M., and L. Mahrt, 1991: A formulation for boundary-layer cloud cover. *Ann. Geophys.*, **9,** 716–724.

FAO-UNESCO, 1979: *Soil Map of the World, 1:5,000,000.* Vol. 7. UNESCO, 117 pp. and 6 plates.

Gallée, H., 1995: Simulation of the mesocyclonic activity in the Ross Sea, Antarctica. *Mon. Wea. Rev.*, **123,** 2051–2069.

——, and G. Schayes, 1994: Development of a three-dimensional meso-gamma primitive equations model, katabatic winds simulation in the area of Terra Nova Bay, Antarctica. *Mon. Wea. Rev.*, **122,** 671–685.

——, J.-P. van Ypersele, T. Fichefet, C. Tricot, and A. Berger, 1991: Simulation of the last glacial cycle by a coupled 2-D climate-ice sheet model. 1: The climate model. *J. Geophys. Res.*, **96,** 13 139–13 161.

Garratt, J. R., 1992: *The Atmospheric Boundary Layer.* University Press, 316 pp.

Holben, B. N., 1986: Characteristics of maximum-value composite images from temporal AVHRR data. *Int. J. Remote Sens.*, **7,** 1417–1434.

Holton, J. R., 1992: *An Introduction to Dynamic Meteorology*. Academic Press, 511 pp.

Kessler, E., 1969: *On the Distribution and Continuity of Water Substance in Atmospheric Circulations. Meteor. Monogr.*, No. 32, Amer. Meteor. Soc., 84 pp.

Klink, K., 1995: Surface aggregation and subgrid-scale climate. *Int. J. Climatol.*, **15,** 1219–1240.

Mandel, M., and Y. Mahrer, 1995: Evaluation of evaporation over Israel as related to surface parameters with a 3-D numerical model. *Extended Abstracts, The Jehuda Neumann Memorial Symp. on Mesoscale Modeling and Climate History*, Jerusalem, Israel, Hebrew University, 77–81.

Morcrette, J.-J., 1984: Sur la paramétrisation du rayonnement dans les modèles de la circulation générale atmosphérique. Thèse de doctorat d'Etat, Univ. des Sci. et Tech. de Lille, Lille, France, 373 pp. [Available from Laboratoire d'Optique Atmosphérique, Université de Lille, F-59655 Villeneuve d'Ascq, France.]

Otterman, J., A. Manes, S. Rubin, P. Alpert, and D. O'C. Starr, 1990: An increase of early rains in southern Israel following land use change? *Bound.-Layer Meteor.*, **53,** 333–351.

Pielke, R. A., 1984: *Mesoscale Meteorological Modeling*. Academic Press, 612 pp.

Pipes, L. A., and L. R. Harvill, 1971: *Applied Mathematics for Engineers and Physicists*. McGraw-Hill, 1015 pp.

Price, J. C., 1984: Land surface temperature measurements from the split-window channels of the *NOAA-7* Advanced Very High Resolution Radiometer. *J. Geophys. Res.*, **89,** 7231–7237.

Rahman, H., B. Pinty, and M. M. Verstraete, 1993: Coupled surface–atmosphere reflectance (CSAR) model. 2. Semiempirical surface model usable with NOAA Advanced Very High Resolution Radiometer data. *J. Geophys. Res.*, **98,** 20 791–20 801.

Richter, W., 1981: *Southern Levant. Land Use. 1:500,000*. Dr. Ludwig Reichert Verlag, 1 sheet.

Stein, U., and P. Alpert, 1993: Factor separation in numerical simulations. *J. Atmos. Sci.*, **50,** 2107–2115.

Steinberger, E. H., and N. Gazit-Yaari, 1996: Recent changes in the spatial distribution of annual precipitation in Israel. *J. Climate*, **9,** 3328–3336.

Tanré, D., C. Deroo, P. Duhaut, M. Herman, J.-J. Morcrette, J. Perbos, and P. Y. Deschamps, 1990: Description of a computer code to simulate the satellite signal in the solar spectrum. *Int. J. Remote Sens.*, **11,** 659–668.

Tricot, C., and A. Berger, 1988: Sensitivity of present-day climate to astronomical forcing. *Long- and Short-Term Variability of Climate*, H. Wanner and U. Siegenthaler, Eds., Lecture Notes in Earth Sciences, Vol. 16, Springer Verlag, 132–152.

Zohary, M., 1981: *Southern Levant (Israel and Adjacent Areas). Vegetation. 1:600,000*. Dr. Ludwig Reichert Verlag, 1 sheet.